Electronic Supplementary Material (ESI) for Journal of Materials Chemistry A.


**Supporting Information**

# Supercapacitor of Extraordinary Cycling Stability and High Rate from Nano-Architectured Polyaniline/Graphene on Janus Nanofibrous Film with Shape Memory

Ali Khosrozadeh[a], Gurankit Singh[a], Quan Wang[b], Gaoxing Luo[c*], Malcolm Xing[a,c*]

[a] *Department of Mechanical Engineering, University of Manitoba, Winnipeg, Manitoba R3T 5V6, Canada*

[b] *Department of Mechanics and Aerospace Engineering, Southern University of Science and Technology, Shenzhen, Guangdong 518055, China*

[c] *Institute of Burn Research, State Key Laboratory of Trauma, Burn and Combined Injury, Southwest Hospital, Third Military Medical University, Chongqing, China*

[*] Corresponding author. E-mail address: malcolm.xing@umanitoba.ca (M. Xing); logxw@yahoo.com (G. Luo).

† Electronic Supporting Information available.

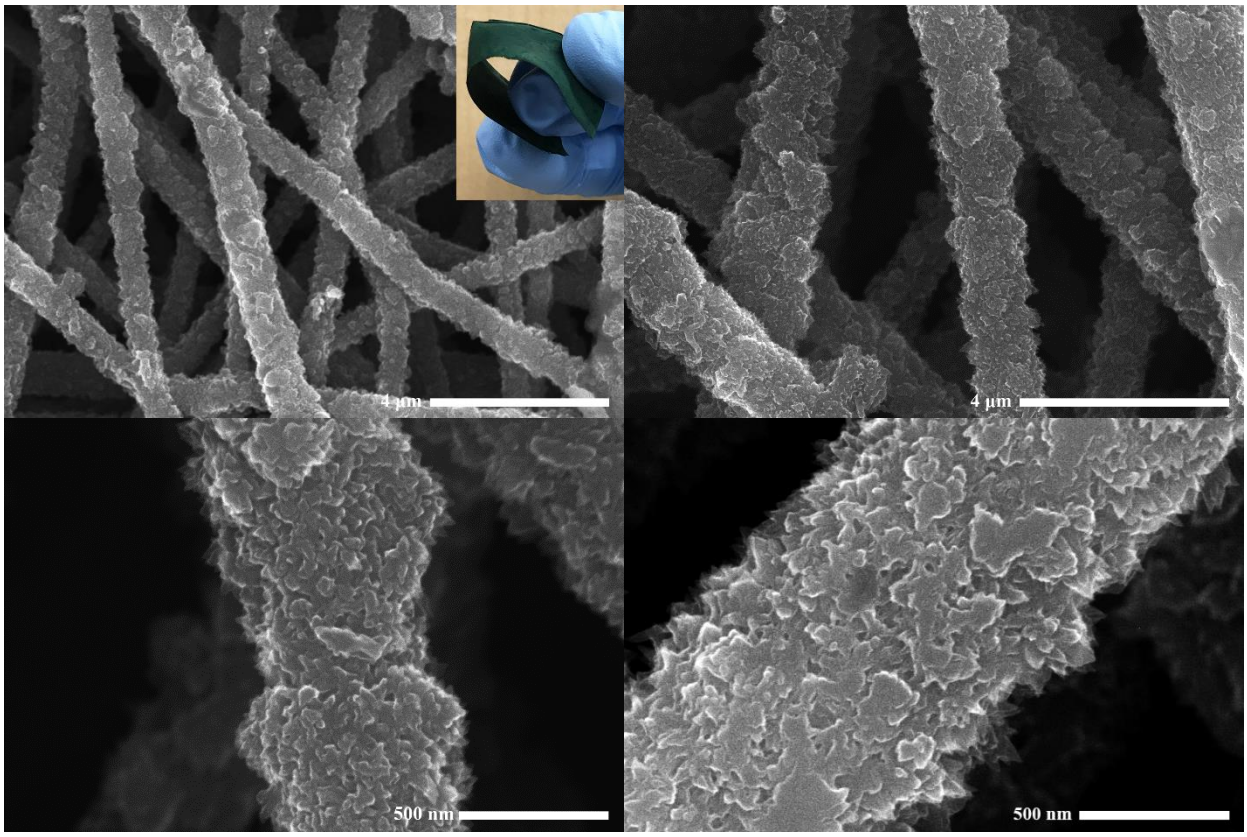


**Fig. S1. SEM images of PVA/PAni films with three coats of PAni; inset is the photo of the flexible PVA/PAni film.**

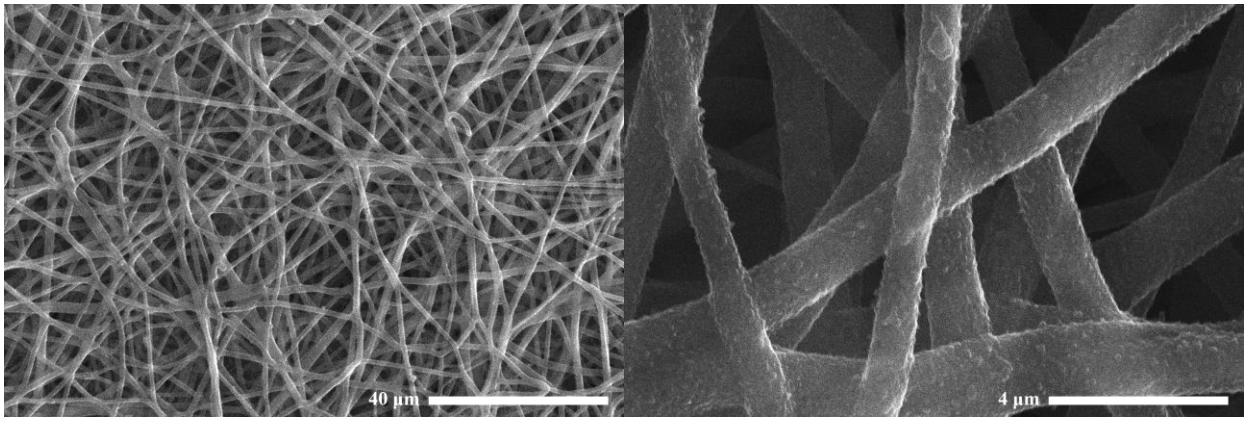


**Fig. S2. SEM images of PVA film coated with PAni after a limited reaction time (20 min), which show the homogenous nucleation of PAni on the nanofibers.**

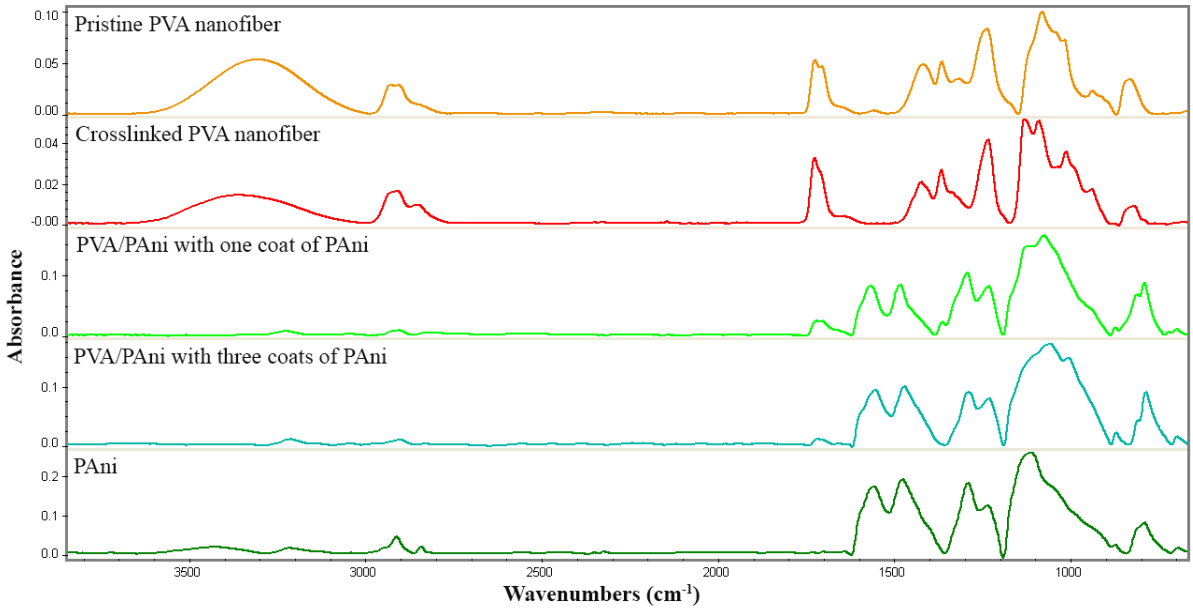


**Fig. S3. FTIR spectra of pristine PVA nanofibers, crosslinked PVA nanofibers, PVA/PAni with one coat of PAni, PVA/PAni with three coats of PAni, and PAni.**

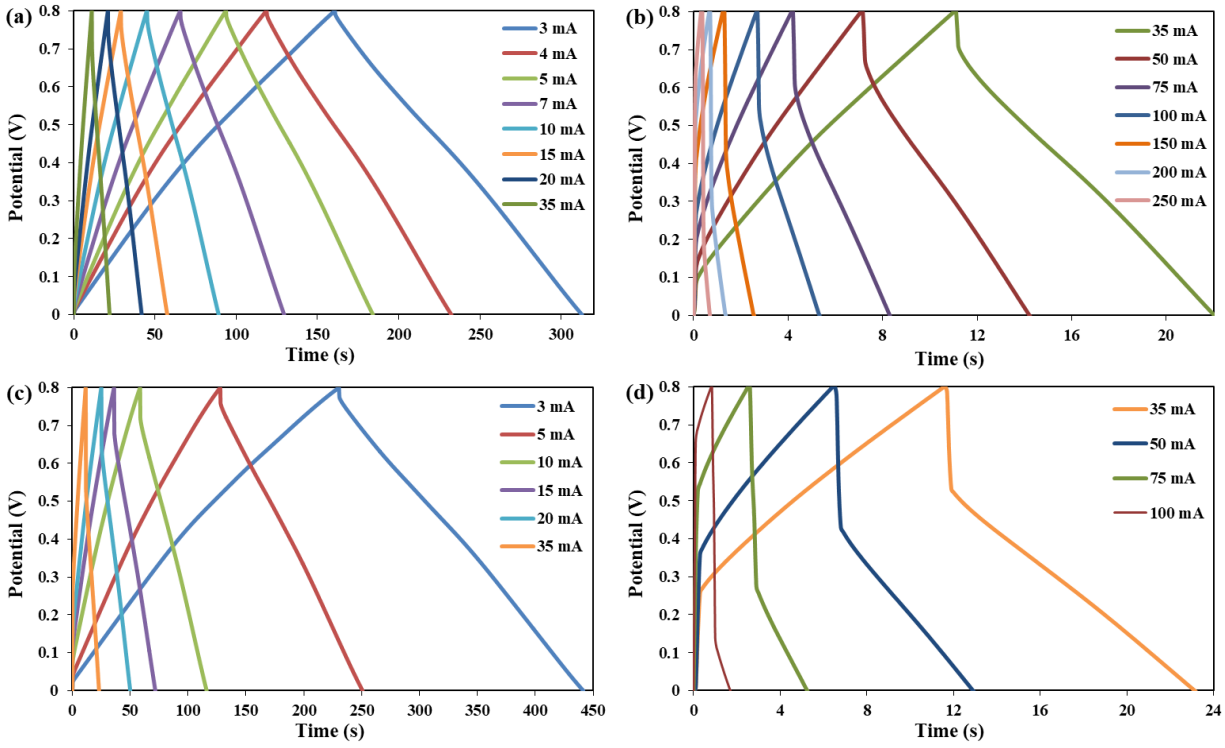


**Fig. S4. The GCD curves of (a-b) SC2 (PVA/G/PAni-3C/G), and (c-d) SC3 (PVA/G/PAni-4C).**

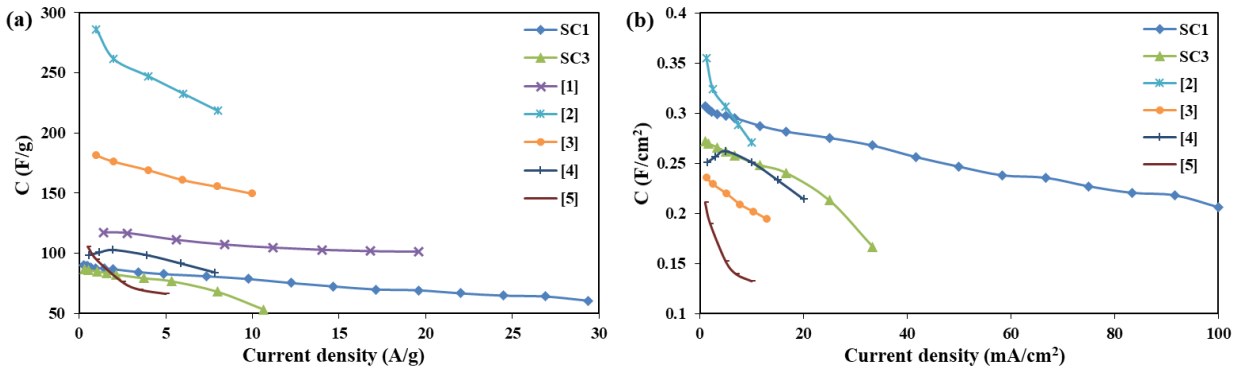


**Fig. S5. Comparison of mass-specific capacitance (a) and area-specific capacitance (b) of SC1 and SC3 with those of previously published PAni-graphene designs (tested in two-electrode system with 1 M $H_2SO_4$). All values are extracted from the references or calculated based on data provided in the references.**

**Table S1. Summary of typical parameters of PAni-graphene SCs provided in Fig. S7.**

| Reference | Electrode mass loading ($mg/cm^2$) | Electrode mass (mg) | Charge-discharge current range (mA) | Equivalent resistance from EIS (ohms) | Capacitance retention, Cycle No. | Description |
|---|---|---|---|---|---|---|
| **SC1** | 1.70 | 5.11 | 3-300 | 0.6 | 75.6%, 88k | PVA/G/PAni-4C/G |
| **SC3** | 1.57 | 4.70 | 3-100 | 5.2 | - | PVA/G/PAni-4C |
| **Ref [1]** | 2.00 | - | 5-70 | - | 83%, 5k | 3D PAni-RGO: PAni absorbed on GO, then reduction |
| **Ref [2]** | 0.62 | 1.24 | 2.5-20 | 14 | 94%, 5k | PAni-RGO coated on carbon fiber cloth |
| **Ref [3]** | 0.65 | 2.60 | 5-50 | ~1 | 80%, 5k | PAni coated on 3D-RGO foam |
| **Ref [4]** | 1.28 | 1.68 | 2-26.4 | 1.8 | 90%, 5k | PAni coated on 3D-RGO film |
| **Ref [5]** | 1.00 | - | - | - | 83%, 2k | Covalently-grafted PAni/GO |

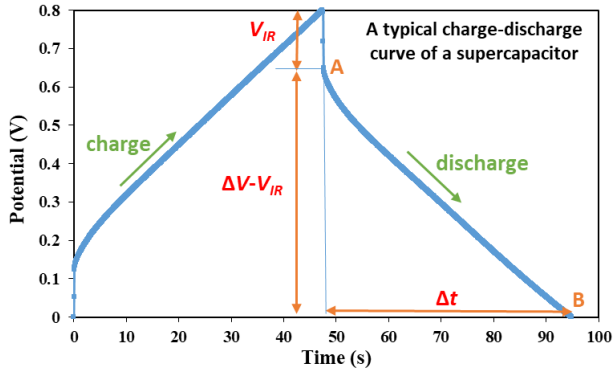


**Fig. S6. Schematic illustration of a typical GCD curve of a SC. Δ*t* and $V_{IR}$ (or ESR as $ESR = V_{IR}/I$ ) are the only parameters that can change during a cycling test and thus affect the cell capacitance (*C*), energy (*E*), and power (*P*) according to $C = I\Delta t/(\Delta V - V_{IR})$ , $E = 0.5I(\Delta V - V_{IR})\Delta t$ , and $P = 0.5I(\Delta V - V_{IR})$ . Δ*t* is the full discharge time, Δ*V* represents the potential window, $V_{IR}$ is the potential drops at the initial discharge stage, and *I* is the constant charge or discharge current.**

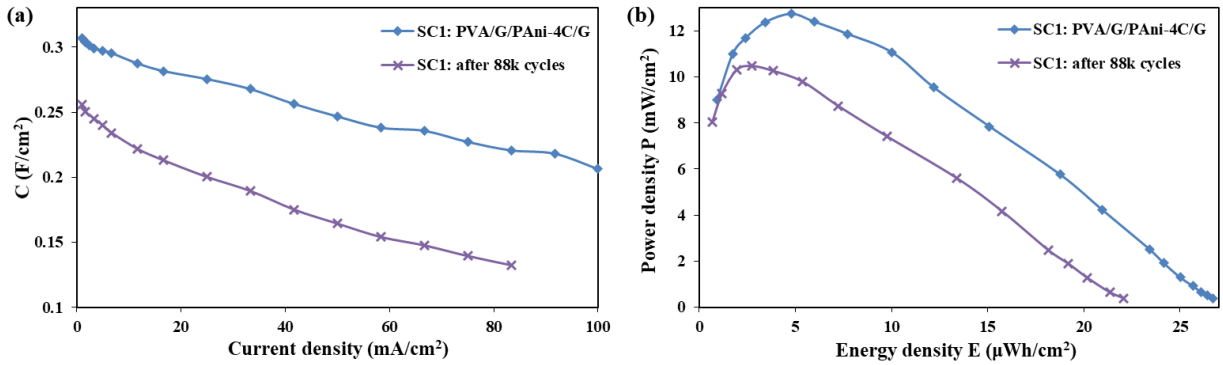


**Fig. S7. Comparison of SC1 performance (obtained from GCD tests) before and after 88k cycles of GCD.**

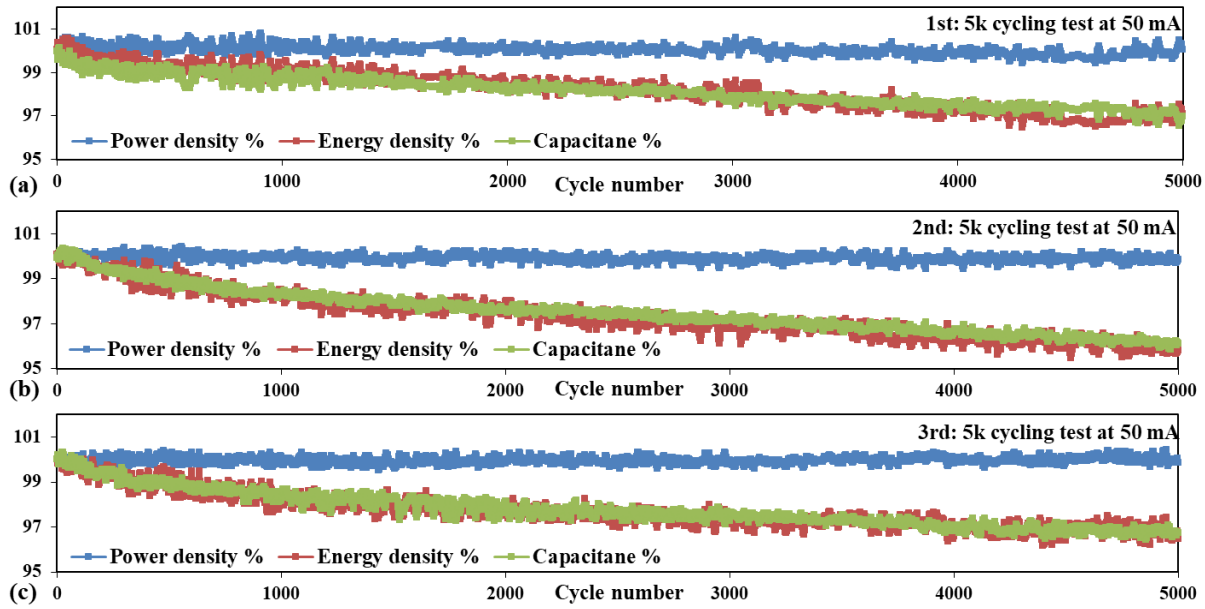

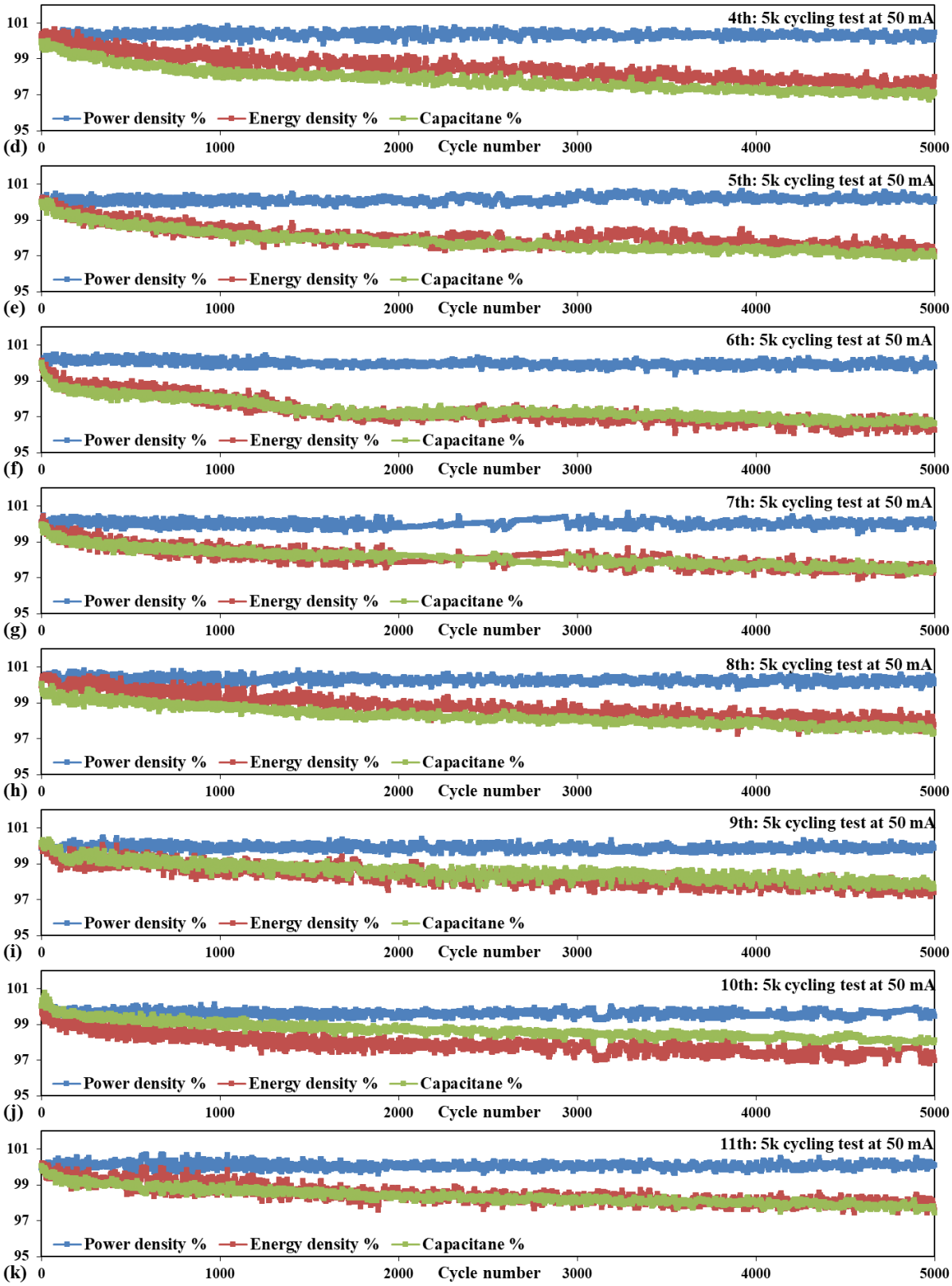
4th: 5k cycling test at 50 mA
Power density %
Energy density %
Capacitane %
Cycle number
(d)
5th: 5k cycling test at 50 mA
(e)
6th: 5k cycling test at 50 mA
(f)
7th: 5k cycling test at 50 mA
(g)
8th: 5k cycling test at 50 mA
(h)
9th: 5k cycling test at 50 mA
(i)
10th: 5k cycling test at 50 mA
(j)
11th: 5k cycling test at 50 mA
(k)
101
99
97
95
0
1000
2000
3000
4000
5000

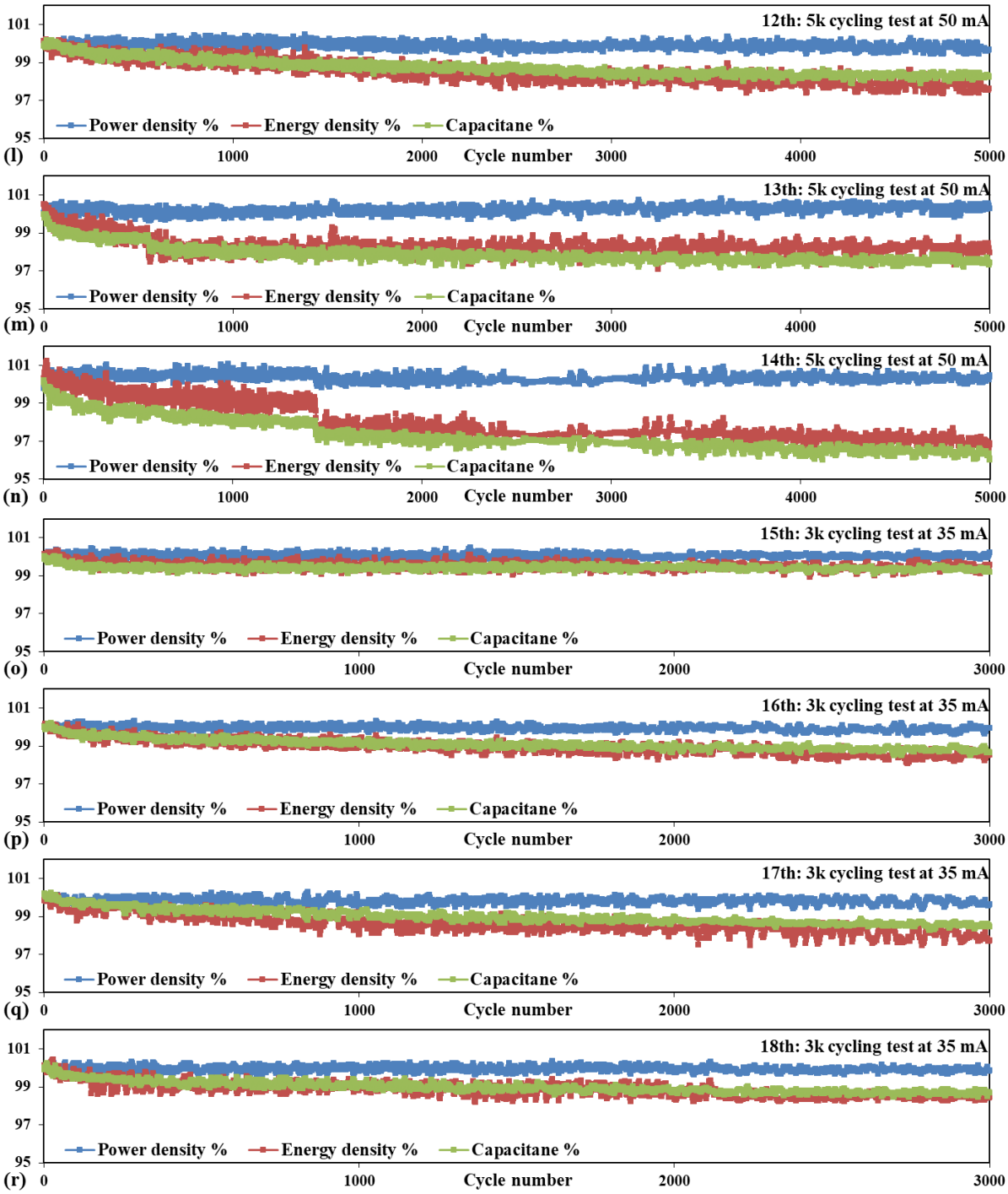
12th: 5k cycling test at 50 mA
Power density %
Energy density %
Capacitane %
Cycle number
(l)
13th: 5k cycling test at 50 mA
(m)
14th: 5k cycling test at 50 mA
(n)
15th: 3k cycling test at 35 mA
(o)
16th: 3k cycling test at 35 mA
(p)
17th: 3k cycling test at 35 mA
(q)
18th: 3k cycling test at 35 mA
(r)

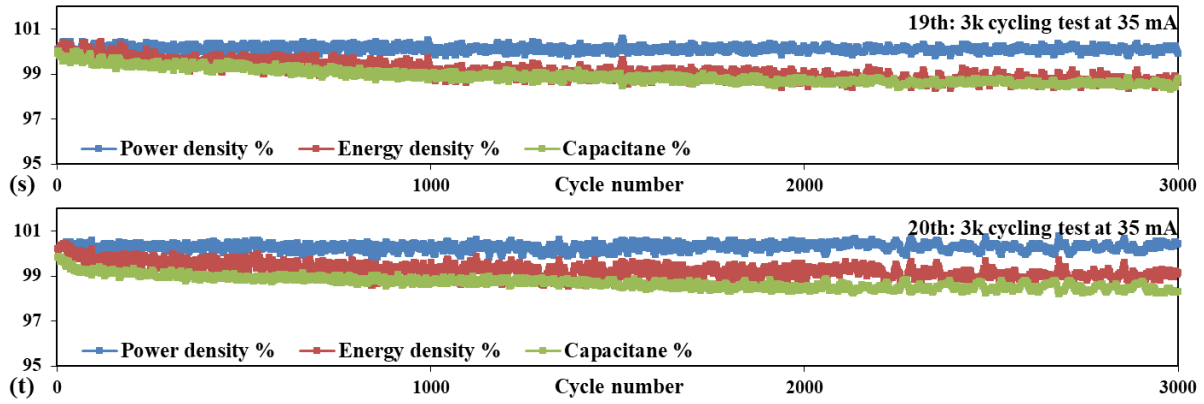


**Fig. S8. Percentages of power density, energy density and capacitance versus cycle number for SC1 for each set of GCD cycling test; (a-n) corresponds to each 5k cycling test conducted at 50 mA and (o-t) each 3k cycling test at 35 mA .**

## Electrochemical Performance of PVA/PAni-3C and PVA/ExG/PAni-3C

PVA/PAni-3C and PVA/ExG/PAni-3C are prepared by growing a PAni on PVA nanofibers and graphene-coated PVA nanofibers, respectively, in a similar way as other samples. As another source of graphene used herein, exfoliated graphene (ExG) is prepared by an electrochemical exfoliation of graphite followed by a post-exfoliation in microwave as reported in our previous work [6]. SEM images of PVA/ExG film and PVA/ExG/PAni-3C film are provided in Fig. S9. As observed in the SEM images of ExG (Fig. S9a-b), the wrinkled structure of graphene sheets in ExG originated from the post-exfoliation by microwave irradiation of electrochemically exfoliated graphite. In addition to wrinkled graphene sheets, smaller graphitic particles (few-layered graphene) observed in Fig. S9a-b are the products of electrochemical exfoliation of graphite [6] which were not fully exfoliated even after post-exfoliation with microwave irradiation. On the other hand, shear-exfoliated graphene sheets retain their in-plane shape (Fig. 2), and thus they are more suitable than ExG as a second coating of graphene owing to their effective overlay of PAni nanowires. The mass loading of active materials (PAni and ExG) on PVA mat for PVA/PAni-3C and PVA/ExG/PAni-3C (three coats of PAni in both cases) are around 1.13 mg/cm$^2$ and 1.46 mg/cm$^2$, respectively. The mass loading of ExG in PVA/ExG/PAni-3C is around 0.4 mg/cm$^2$.

The spectrum of PVA/ExG film in Fig. S10 gives all characteristic peaks of crosslinked PVA nanofiber. Although most of infrared radiation, are absorbed by ExG in FTIR spectra of films coated with ExG, major peaks can still be observed after baseline correction of each spectrum. In addition, the peak at 1574 cm$^{-1}$ is attributed to aromatic C=C stretching bond of graphene. Similar to PVA/PAni, the spectra of PVA/ExG/PAni with one or three coats of PAni also confirm the successful decoration of PAni on PVA/ExG films.

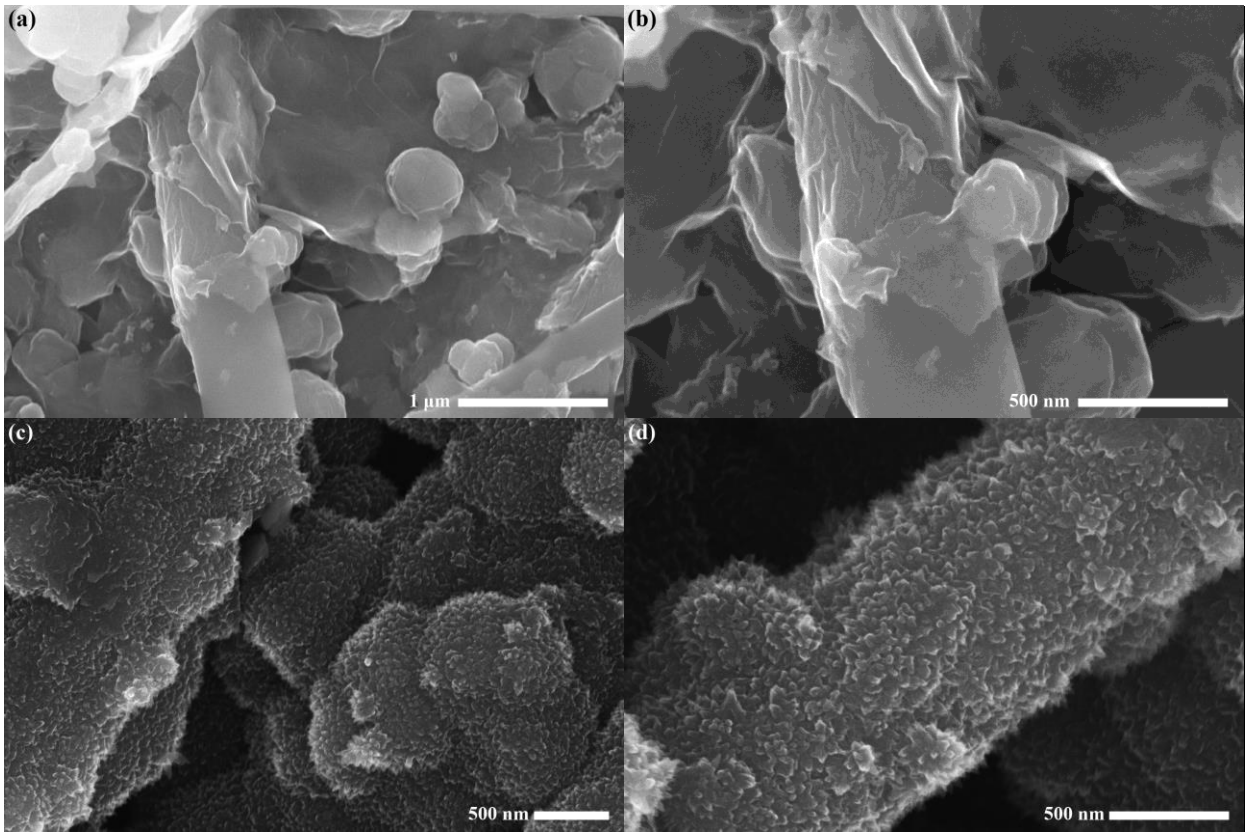


**Fig. S9. SEM images of (a-b) PVA/ExG film and (c-d) PVA/ExG/PAni-3C film.**

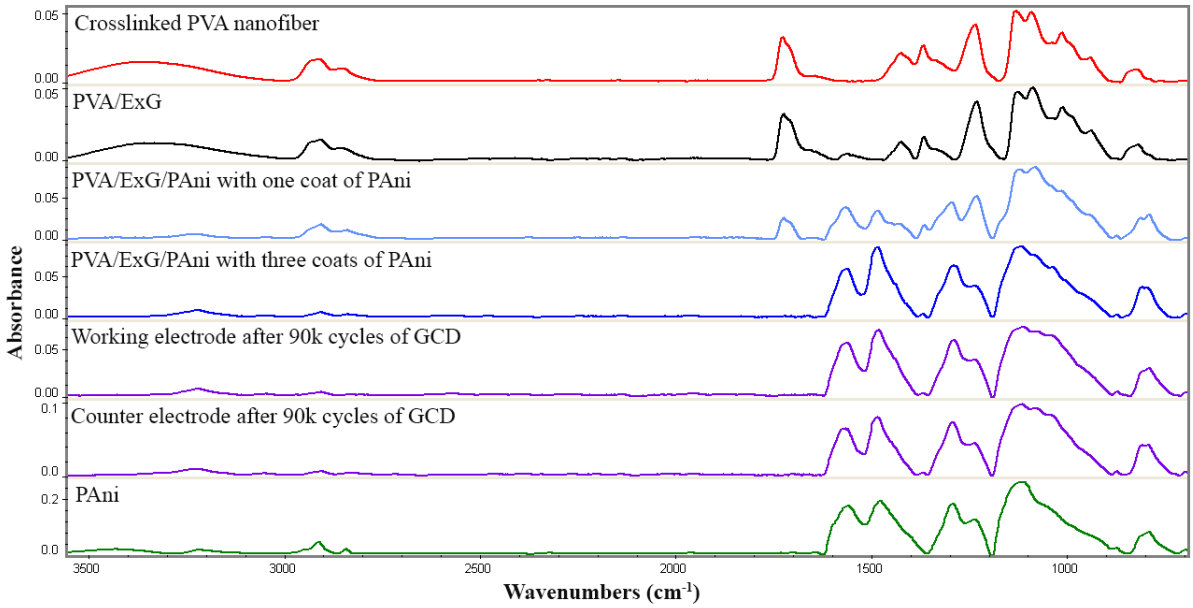


**Fig. S10. FTIR spectra of crosslinked PVA nanofiber, PVA/ExG, PVA/ExG/PAni with one coat of PAni, PVA/ExG/PAni with three coats of PAni, PVA/ExG/PAni (working electrode after 90k cycles of GCD), PVA/ExG/PAni (counter electrode after 90k cycles of GCD), and PAni.**

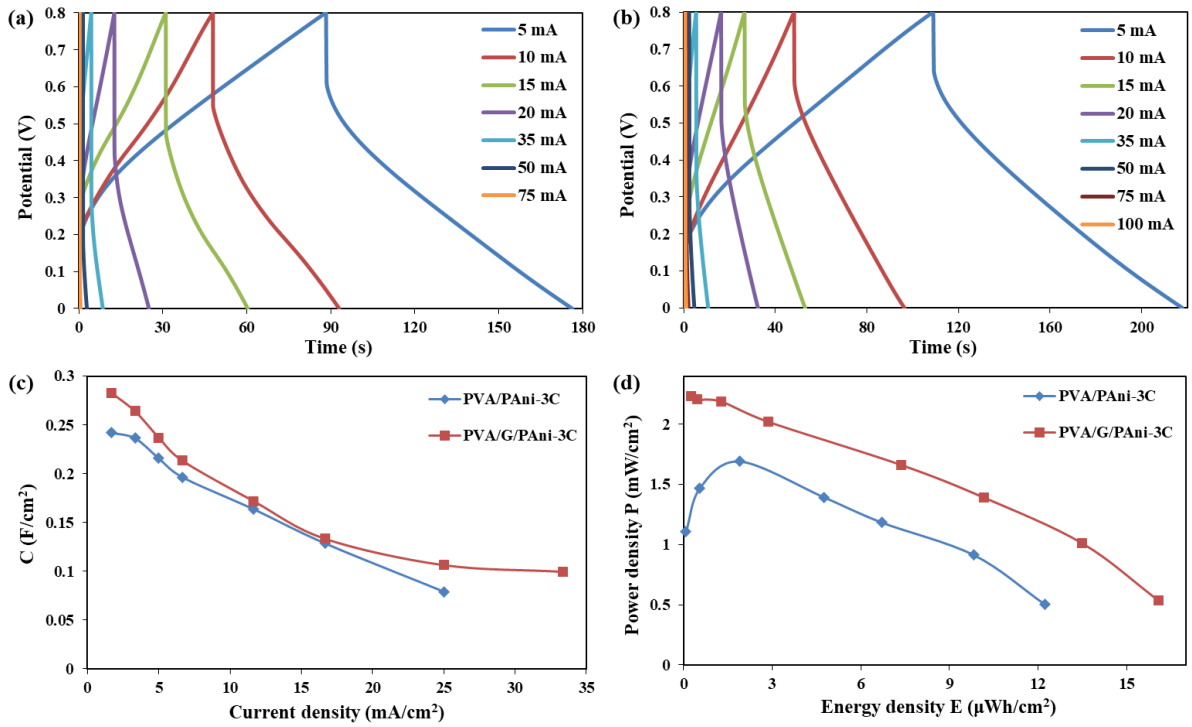


**Fig. S11. The GCD curves of assembled SCs from films of (a) PVA/PAni-3C, and (b) PVA/ExG/PAni-3C; (c) Specific capacitance versus areal current density (per area), (d) power density versus energy density (per area), for PVA/PAni-3C and PVA/ExG/PAni-3C.**

According to Fig. S11, the assembled SC from PVA/ExG/PAni-3C exhibits better areal specific capacitance and areal energy and power densities than those of PVA/PAni-3C. However, PVA/ExG/PAni-3C still suffers from a limited rate capability and large potential drops similar to SC3. The primary role of graphene is to enhance cycling stability of PAni as discussed in the paper. Thus the cycling performance of the assembled SC from PVA/ExG/PAni-3C was extensively investigated to prove the hypothesis that PVA nanofiber together with graphene contribute to the stability of PAni as discussed in the paper.

To investigate the cycling performance of the assembled SC from PVA/ExG/PAni-3C film, 90k cycles of GCD at 35 mA are carried out (a series of 15 consequent 6k cycles with approximately 4h rest period between each 6k cycling test). During the four-hour gap, a series of GCD, EIS, and CV tests are carried out on the SC. The areal specific capacitance, areal energy density, and areal power density, obtained from GCD tests at different currents (10, 20, 35, 50 mA), tested after each 6k cycles, are illustrated in Fig. S12a-c, respectively. It is seen that the capacitance, energy density, and power density are steady up to 84k cycles of GCD for all the currents (10-50 mA). This shows that the fabricated SC can operate up to 84k cycles of charge and discharge. In addition, EIS tests presented in the form of Nyquist plots and GCD curves tested at 10 mA and 35 mA, tested after each set of cycling test, are shown in Fig. S12d-f, respectively. The GCD curves and Nyquist plots also confirm the remarkable cycling stability of the fabricated SC up to 84k cycles.

Fig. S12d and e indicate that the performance of the SC declines dramatically during the 15$^{th}$ 6k cycling test (note: in GCD, a larger potential drop and smaller discharge time are indications of inferior performance; EIS: a larger diameter of the semicircle and more oblique low-frequency line are indications of inferior performance). Furthermore, EIS tests in Fig. S12d reconfirm that the SC based on PVA/ExG/PAni-3C exhibits better capacitive performance than PVA/PAni.

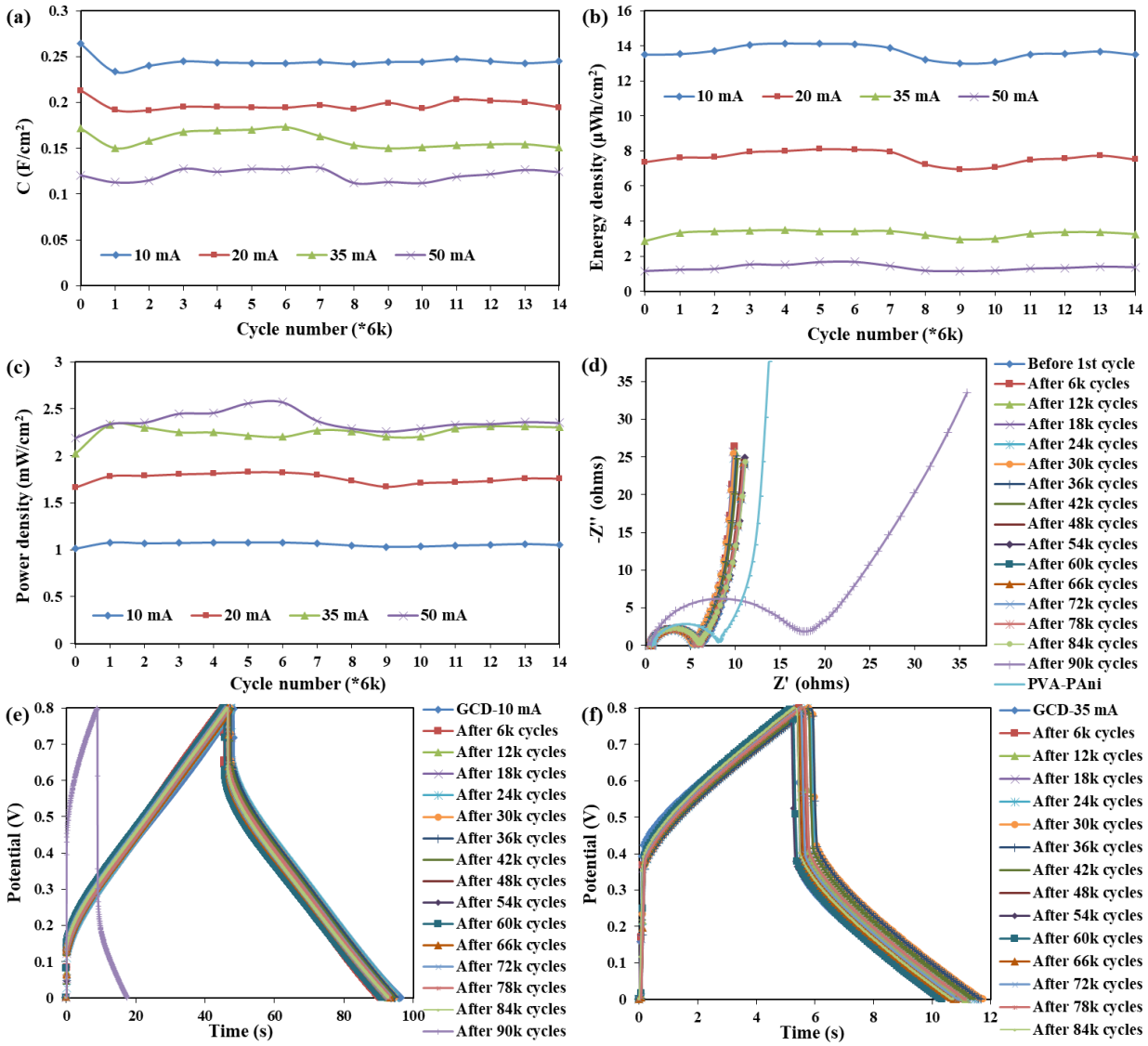


**Fig. S12. Performance of the assembled PVA/ExG/PAni-3C SC tested after each 6k cycling test (totally 90k cycles of GCD at 35 mA); (a) areal specific capacitance versus cycles, (b) areal energy density versus cycles, and (c) areal power density versus cycles, obtained from GCD tests at different currents (10, 20, 35, 50 mA); (d) Nyquist plots obtained from EIS tests after each 6k cycling test (along with Nyquist plots for the PVA/PAni SC); (e) GCD curves tested at 10 mA after each 6k cycling test; (f) GCD curves tested at 35 mA after each 6k cycling test.**

The areal specific capacitance, areal energy density, areal power density, ESR, and discharge time, for the whole 90k cycles of GCD at 35 mA, are illustrated in Fig. S13a-e, respectively. According to the discharge time and ESR curves, two phases can be observed for cycling behavior of each 6k cycling test: a transient phase (with sharp variations in parameters) up to around 500th cycle, and a steady state (with a very small rate of change in parameters) afterward. According to Fig. S13, the steady-state values of the capacitance for every 6k cycling test remain unchanged (0.15 $F/cm^2$) during the whole 84k cycles. The steady-state values of the energy density and power density for each 6k cycling test are around 3.0-3.7 $\mu Wh/cm^2$ and 2.2-2.4 $mW/cm^2$, respectively. Overall, the retention of the steady-state values of the capacitance, energy density, and power density were found to be 97%, 100%, and 99%, respectively. The fact that the fabricated SC can be operated up to 84k cycles without any pronounced decline in the performance implies an outstanding cycling stability of this SC device.

The initial sharp changes in the ESR and the discharge time during the transient stage indicates the performance recovery (Fig. S13d and e), which may be attributed to the regulation of ion transport to active sites as well as regulation of reversible reduction-oxidation reactions in PAni. Upon the initiation of charge-discharge cycles, it takes some time for electrolyte ions to effectively diffuse into the active sites from their previous equilibrium state [6-7]. The duration of the transient phase (or the performance recovery stage) depends on factors such as experimental conditions, the sample type, and type of electrochemical tests carried out on the SC right before the initiation of cycling tests (which is the case herein). Some tests might be detrimental to PAni, such as performing a test with a large potential window since it enforces PAni to experience various oxidation states. After each 6k cycling test and before the next set of cycling test (during the four-hour rest period), we carried out EIS, GCD tests (0-0.8 V), and CV tests (-0.8-0.8 V), respectively, to track the state of electrodes during cycling. CV tests were carried out from -0.8-0.8 V to probe any change in symmetry (both electrodes being in similar state) or shape of CV when the positive and negative electrodes are exchanged (i.e. -0.8-0 V). For example, the unchanged and symmetrical shape of CV curves tested at 10 mV/s after each set of cycling test confirms the cycling stability of the device up to 84k cycles (Fig. S14a). By performing another GCD test at 35 mA after CV tests (Fig. S14b), the adverse effect of CV tests with a larger potential window (-0.8-0.8 V) was observed (the late GCD curve shows a larger potential drop and a smaller discharge time). The voltage difference between the positive and negative electrodes changes from -0.8 to 0.8 V, implying that each electrode experiences 1.6 V potential change. Therefore, it takes several cycles for electrode materials to recover from the adverse effect of a large potential change in electrodes and adapt to a different testing condition. On the other hand, the transient phase of SC1 shown in Fig. 6 (or Fig. S8) are much shorter since no CV tests (-0.8-0.8 V) were conducted during the rest period between each set of cycling test. According to Fig. S13, all 14 sets of 6k cycling test show this performance recovery in the form of a decrease in the ESR (or potential drop) and/or an increase in the discharge time. These changes are sharp during the transient stage up to around 500th cycle and steady afterward. It should be noted that an increase

in the discharge time and a reduction in the potential drop lead to a negligible change in the capacitance ( $C = I\Delta t/(\Delta V - V_{IR})$ ) during 6k cycles for all 14 sets of cycling tests, as seen in Fig. S13. The energy density is increased for all 14 sets of cycling tests because of a decrease in the potential drop and an increase in the discharge time are both in favor of the energy density ( $E = 0.5I(\Delta V - V_{IR})\Delta t$ ). In addition, the power density is increased for all 14 sets of cycling tests since a decrease in the potential drop is in favor of the power density ( $P = 0.5I(\Delta V - V_{IR})$ ).

The rapid decline in the capacitive performance during the 15$^{th}$ 6k cycling test (Fig. S13) may be attributed to water evaporation from the assembled SC and/or counterion drain effect (less and less anions can penetrate into PAni matrix due to the irreversible insertion/de-insertion of counterions after repeated charge/discharge cycling [8]). Additionally, the shape of the 15$^{th}$ CV curve in Fig. S14a clearly indicates that the capacitive performance of the SC has diminished after the 15$^{th}$ 6k cycling test.

After the 15$^{th}$ cycling test, the SC was disassembled and the morphology of the electrodes were observed using SEM. According to the morphologies of the working electrode and counter electrode after the cycling test (Fig. S15), the surface of individual nanofibers are less porous. Despite this minor alternation in nanostructure of the electrodes, the active materials are still well embedded on individual PVA nanofibers. Additionally, the FTIR spectra of the working electrode and counter electrode after 90k cycles of GCD (Fig. S10) are similar to spectrum of PVA/ExG/PAni film and show all the expected characteristic peaks of PAni.

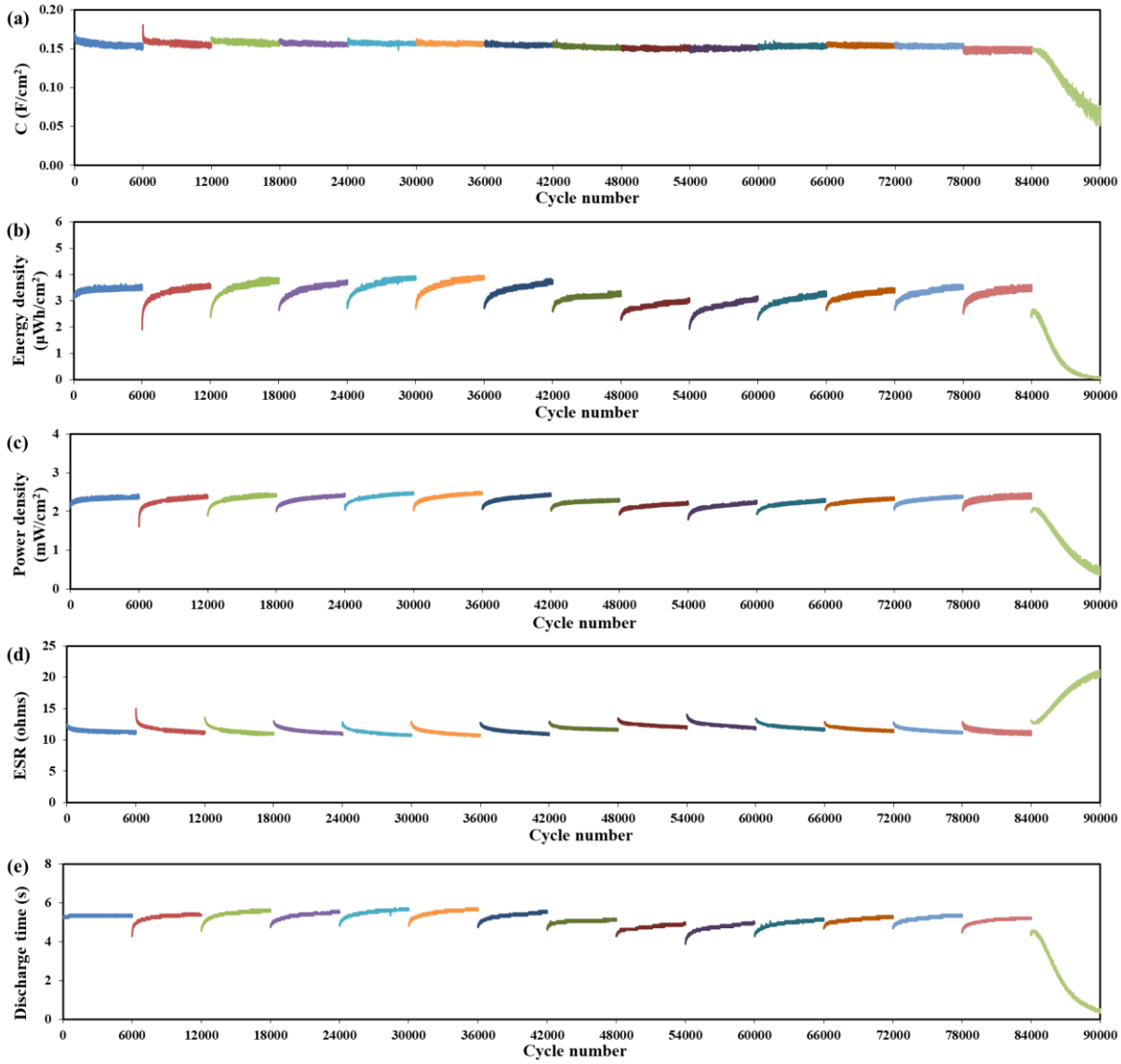


**Fig. S13. Performance of the fabricated SC from PVA/ExG/PAni-3C for 90k cycles of GCD at 35 mA; (a) Areal specific capacitance, (b) areal energy density, (c) areal power density, (d) ESR, and (e) discharge time, versus cycle number.**

The rapid decline in the capacitive performance during the 15$^{th}$ 6k cycling test (Fig. S13) may be attributed to water evaporation from the assembled SC and/or counterion drain effect (less and less anions can penetrate into PAni matrix due to the irreversible insertion/de-insertion of counterions after repeated charge/discharge cycling [8]). Additionally, the shape of the 15$^{th}$ CV curve in Fig. S14a clearly indicates that the capacitive performance of the SC has diminished after the 15$^{th}$ 6k cycling test.

After the 15$^{th}$ cycling test, the SC was disassembled and the morphology of the electrodes were observed using SEM. According to the morphologies of the working electrode and counter electrode after the cycling test (Fig. S15), the surface of individual nanofibers are less porous. Despite this minor alternation in

nanostructure of the electrodes, the active materials are still well embedded on individual PVA nanofibers. Additionally, the FTIR spectra of the working electrode and counter electrode after 90k cycles of GCD (Fig. S10) are similar to spectrum of PVA/ExG/PAni film and show all the expected characteristic peaks of PAni.

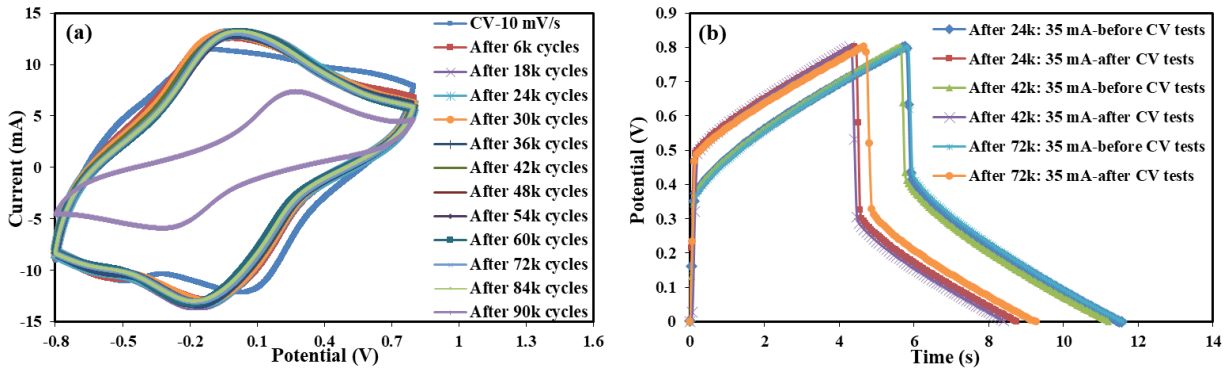


**Fig. S14. (a) CV curves of the SC from PVA/ExG/PAni-3C tested at 10 mV/s after each 6k cycling test. (b) Comparison of GCD curves tested at 35 mA before and after CV tests, performed on the SC during the rest time after the 4$^{th}$, 7$^{th}$, and 12$^{th}$ 6k cycling tests.**

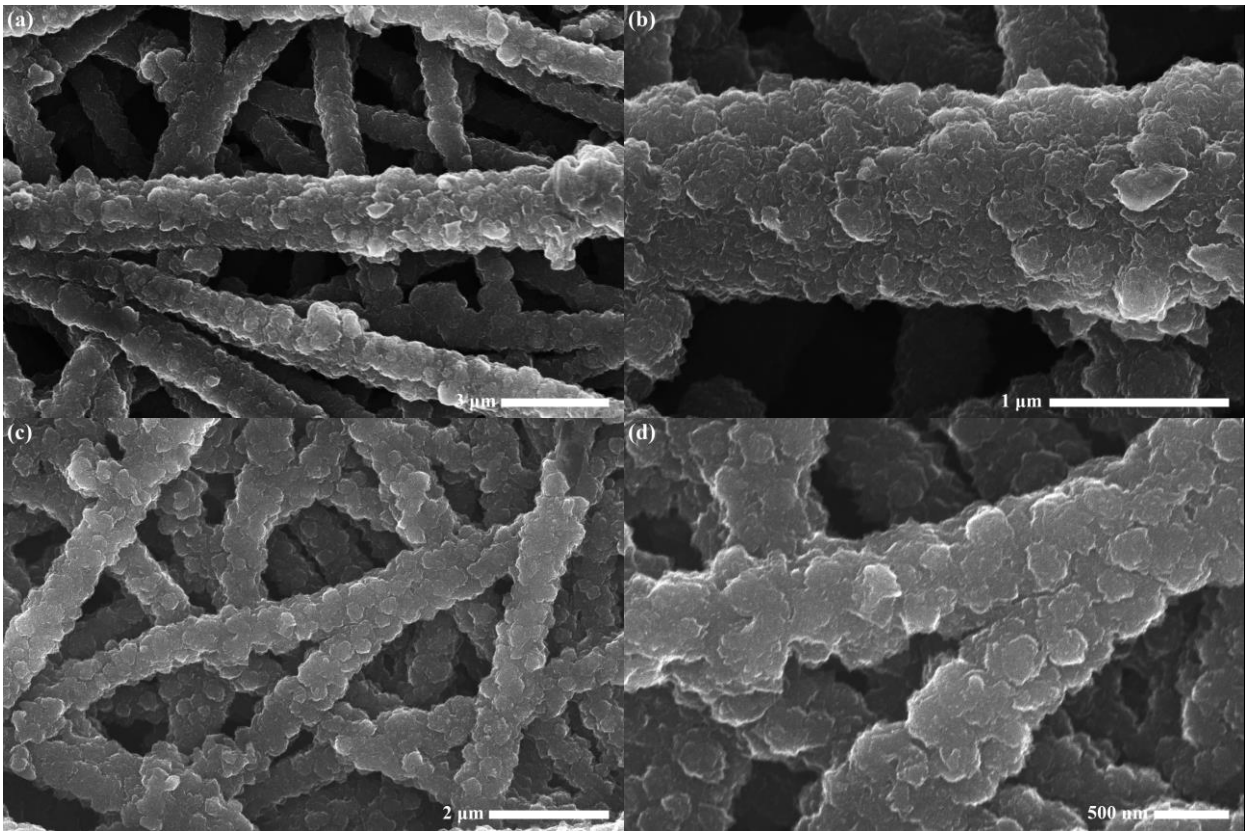


**Fig. S15. SEM images of (a-b) working electrode and (c-d) counter electrode following 90k cycles of GCD at 35 mA (PVA/ExG/PAni-3C).**

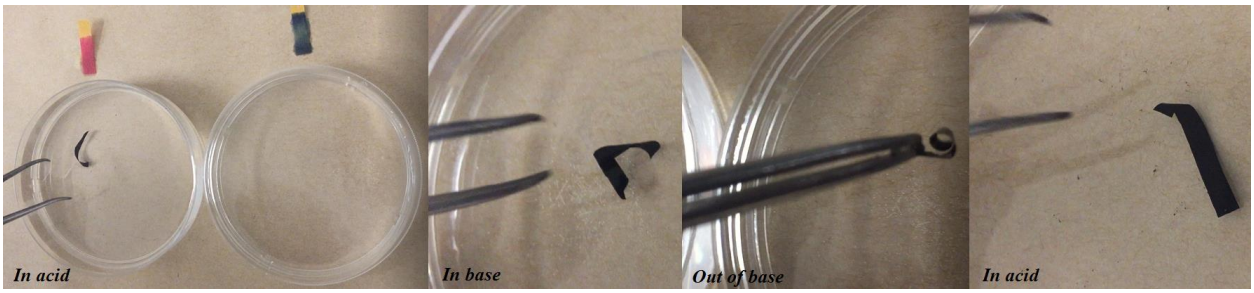


**Fig. S16. The pH-driven shape memory phenomenon observed for the PVA/ExG/PAni-3C film. Due to the nanostructured asymmetry of each side of the ribbon, its curvature changes and it curls up when it is placed from 1 M $H_2SO_4$ to 1 M NaOH; and it recovers its original shape upon returning to 1 M $H_2SO_4$ (See video #2).**

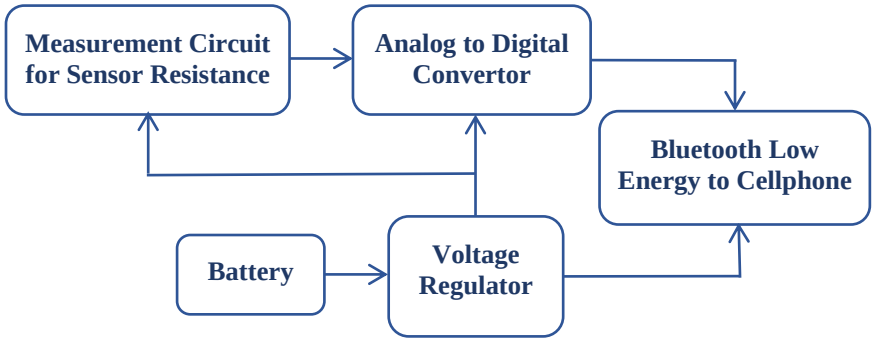


**Fig. S17. The block diagram of the wireless resistance monitoring setup used for the real-time sensing of HCl vapor and ammonia.**

## References

(1) Wu, J.; Zhang, Q. e.; Wang, J.; Huang, X.; Bai, H., A self-assembly route to porous polyaniline/reduced graphene oxide composite materials with molecular-level uniformity for high-performance supercapacitors. *Energy Environ. Sci.* 2018**,** *11* (5), 1280-1286.

(2) Yu, P.; Li, Y.; Zhao, X.; Wu, L.; Zhang, Q., Graphene-Wrapped Polyaniline Nanowire Arrays on Nitrogen-Doped Carbon Fabric as Novel Flexible Hybrid Electrode Materials for High-Performance Supercapacitor. *Langmuir* 2014**,** *30* (18), 5306-5313.

(3) Yu, P.; Zhao, X.; Huang, Z.; Li, Y.; Zhang, Q., Free-Standing Three-Dimensional Graphene and Polyaniline Nanowire Arrays Hybrid Foams for High-Performance Flexible and Lightweight Supercapacitors. *J. Mater. Chem. A* 2014**,** *2* (35), 14413-14420.

(4) Meng, Y.; Wang, K.; Zhang, Y.; Wei, Z., Hierarchical Porous Graphene/Polyaniline Composite Film with Superior Rate Performance for Flexible Supercapacitors. *Adv. Mater.* 2013**,** *25* (48), 6985-6990.

(5) Li, Z.-F.; Zhang, H.; Liu, Q.; Liu, Y.; Stanciu, L.; Xie, J., Covalently-grafted polyaniline on graphene oxide sheets for high performance electrochemical supercapacitors. *Carbon* 2014**,** *71*, 257-267.

(6) Khosrozadeh, A.; Darabi, M. A.; Xing, M.; Wang, Q., Flexible Electrode Design: Fabrication of Freestanding Polyaniline-Based Composite Films for High-Performance Supercapacitors. *ACS Appl. Mater. Interfaces* 2016**,** *8* (18), 11379-11389.

(7) Khosrozadeh, A.; Darabi, M. A.; Wang, Q.; Xing, M., Polyaniline nanoflowers grown on vibration-isolator-mimetic polyurethane nanofibers for flexible supercapacitors with prolonged cycle life. *J. Mater. Chem. A* 2017**,** *5* (17), 7933-7943.

(8) Song, Y.; Liu, T.-Y.; Xu, X.-X.; Feng, D.-Y.; Li, Y.; Liu, X.-X., Pushing the Cycling Stability Limit of Polypyrrole for Supercapacitors. *Adv. Funct. Mater.* 2015**,** *25* (29), 4626-4632.